Development and Characterisation of Acoustofluidic Devices Using Detachable Electrodes Made from PCB

Roman Mikhaylov[1], Fangda Wu[1], Hanlin Wang[1], Aled Clayton[2], Chao Sun[3], Zhihua Xie[4], Dongfang Liang[5], Yinhua Dong[6], Fan Yuan[7], Despina Moschou[8], Zhenlin Wu[9], Ming Hong Shen[10], Jian Yang[10], Yongqing Fu[11], Zhiyong Yang[12], Christian Burton[1,2], Rachel J. Errington[2], Marie Wiltshire[2], Xin Yang[1]

[1] Department of Electrical and Electronic Engineering, School of Engineering, Cardiff University, Cardiff CF24 3AA, UK

[2] Tissue Micro-Environment Group, Division of Cancer & Genetics, School of Medicine, Cardiff University, Cardiff CF14 4XN, UK

[3] School of Life Sciences, Northwestern Polytechnical University, 710129, P.R. China

[4] Department of Civil Engineering, School of Engineering, Cardiff University, Cardiff CF24 3AA, UK

[5] Department of Engineering, University of Cambridge, Cambridge CB2 1PZ, UK

[6] Department of Neurology, Tianjin 4th Centre Hospital Affiliated to Nankai University, 300140, P.R. China

[7] Department of Biomedical Engineering, School of Engineering, Duke University, NC 27708-0281, USA

[8] Centre for Biosensors, Bioelectronics and Biodevices (C3Bio) and Department of Electronic & Electrical Engineering, University of Bath, Bath BA2 7AY, UK

[9] School of Optoelectronic Engineering and Instrumentation Science, Dalian University of Technology, 116023, P.R. China

[10] Preclinical Studies of Renal Tumours Group, Division of Cancer and Genetics, School of Medicine, Cardiff University, Cardiff CF14 4XN, UK

[11] Faculty of Engineering and Environment, Northumbria University, Newcastle Upon Tyne, Newcastle NE1 8ST, UK

[12] School of Mechanical Engineering, Tianjin University, 300072, P.R. China

Abstract:

Acoustofluidics has been increasingly applied in biology, medicine and chemistry due to its versatility in manipulating fluids, cells and nano-/micro-particles. In this paper, we develop a novel and simple technology to fabricate a surface acoustic wave (SAW)-based acoustofluidic device by clamping electrodes made using a printed circuit board (PCB) with a piezoelectric substrate. The PCB-based SAW (PCB-SAW) device is systematically characterised and benchmarked with a SAW device made using the conventional photolithography process with the same specifications. Microparticle manipulations such as streaming in droplets and patterning in microchannels were demonstrated in the PCB-SAW device. In addition, the PCB-SAW device was applied as an acoustic tweezer to pattern lung cancer cells to form three or four traces inside the microchannel in a controllable manner. Cell viability of ~97% was achieved after acoustic manipulation

using the PCB-SAW device, which proved its ability as a suitable tool for acoustophoretic applications.

Introduction

Acoustophoresis is a technique well-known for actuating and manipulating micro[1]-/nano[2,3]- particles using acoustic waves. Its applications have been demonstrated in a wide-range of biomedical applications such as separating blood cells and platelets[4], separating circulating tumour cells from whole blood[5,6], isolating exosomes[7,8], washing[9] and coating of cells[10], handling liquid [11] and versatile manipulations of micro-objects[12–20], alongside the continuous development of acoustophoretic theories[21–24] and simulations[25–27]. Acoustophoretic devices using either bulk acoustic waves (BAWs)[4,28] or surface acoustic waves (SAWs) produce an acoustic pressure gradient and streaming within a fluid, thus achieving the capability of actuating micro-/nano-particles inside. SAW-based devices have been intensively investigated in manipulating biological cells because of their versatility and being less-dependent on the acoustic properties of the microchannel material when compared to those made using BAWs[28].

SAW devices are generally fabricated by patterning an interdigitated transducer (IDT)[17] onto piezoelectric substrate such as lithium niobate ($LiNbO_3$). IDTs typically have two comb-shaped arrays of metallic electrodes, which are driven by radio frequency (RF) signals to produce SAWs. The fabrication process of SAW devices typically employs photolithography, which includes the following steps: 1. mask design and manufacturing; 2. spin-coating photoresist onto $LiNbO_3$; 3. mask aligning for patterning with UV light; 4. metal layer deposition; 5. lift-off process to form the IDT[17]. The brittle[29] bulk $LiNbO_3$ substrate is vulnerable during manufacturing and operation. Furthermore, the SAW

63 device made by photolithography is a one-off component, any modification will require to
64 go through the entire aforementioned manufacturing processes again. It is also difficult to
65 repair a damaged substrate (i.e., scratches). The facilities and skills required for making
66 IDTs limit the use of SAW devices. To address these issues and simplify the process, the
67 creation of shear-SAWs has been demonstrated on the surface of $LiNbO_3$ by stacking
68 aluminum foil strips onto the substrate[30]. IDTs have also been created by pouring low-
69 melting point metal into an IDT mold made by PDMS[31]. Superstrates have also been
70 implemented on the conventional SAW devices to allow their reuse for different
71 applications[32].

72 Interdigital electrodes (IDEs), with a similar pattern as that in SAW devices, have also
73 been fabricated on printed circuit boards (PCBs). They have been applied in various
74 applications such as moisture sensing[33], water level measurements[34], electro wetting[35],
75 biosensing[36] and even cell manipulation[37]. A standard PCB laminate consists of a layer
76 of thin copper foil and an insulating layer typically laminated together with glass reinforced
77 epoxy resin (FR4). Further choices for core materials are commercially available such as
78 PET (Polyethylene terephthalate), flexible polyimide or Teflon. This allows versatility
79 based on different applications. The fabrication of IDEs on the PCB by metallisation of
80 the copper layer is routinely employed within the industry with a wide variety of gold or
81 silver electroplating processes commercially available.

82 In this work, we demonstrated a novel SAW device fabrication technique done by
83 mechanically clamping IDEs on the PCB to a $LiNbO_3$ wafer. This PCB-based SAW (PCB-

SAW) device was characterised and benchmarked against an IDT with the same specifications made using the conventional photolithography process. The PCB-SAW device was used as an acoustic tweezer to actuate and pattern both polystyrene microspheres and cancer cells. The proof-of-concept demonstrated that the simple mechanical clamping technique could be applied as an alternative to the conventional photolithography, by transferring the photolithography effort in fabricating SAW devices to the mature PCB manufacturing industry.

Methods and materials

Design and working mechanism

The schematic illustration of the PCB-SAW device shown in Figs. 1a and 1b consists of six components: a base plate, a $LiNbO_3$ wafer, a PCB with a pair of patterned IDEs, a clamp, a pressure ring and a microchannel. The base plate supports the $LiNbO_3$ wafer and is bolted with the clamp to apply clamping force between the PCB and the $LiNbO_3$ wafer via the pressure ring. Once a proper clamping force is applied by fastening the four screws on the clamp, the pair of IDEs make good contacts to the $LiNbO_3$ wafer to couple RF signals that generate counter-propagating SAWs to form standing SAWs (SSAWs) between the two IDEs. The microchannel is bonded to the $LiNbO_3$ wafer at the middle between the two IDEs for handling fluid samples. Depending on the size of microparticles and other application parameters, the SAW wavelength can be customised by producing PCBs with alternative IDEs specifications.

104

105 **PCB-SAW fabrication and experimental setup**

106 The PCB was designed using the Eagle software (Autodesk, US) and manufactured
107 externally (circuitfly.com). All the design files are accessible as supporting files of this
108 work. The PCB design had a conventional IDT pattern for SAW devices with the
109 wavelength of 200 μm, corresponding to Rayleigh mode frequency of 19.9 MHz. This is
110 based on that the speed of sound in the $LiNbO_3$ is 3,980 m/s. Each IDT consists of 40
111 pairs of 10 mm (aperture size) long finger electrodes. The manufactured single-sided PCB
112 is shown in Fig. 2a. The thickness of the PCB laminate is 1.6 mm with the IDE layer
113 thickness of 34.8 μm of copper. The IDEs and the buses are exposed without pasted
114 solder mask. The PCB dimensions are 10 cm (L) × 10 cm (W) with a milled open window
115 of 3.5 cm (L) × 1.5 cm (W) at the centre for accommodating the microchannel. Alignment
116 markers (holes and lines) are present on the PCB to help align the microchannel and the
117 $LiNbO_3$ wafer. A microscope was used to check the IDE manufacturing quality (Fig. S1).
118 Two coaxial cables were soldered to the bus pads at the edges of the PCB for signal
119 transmissions.

120 Before the assembly process, both the PCB IDEs and a 3-inch, 500-μm thick, 128-deg-
121 rotated Y-cut X-propagation $LiNbO_3$ wafer were thoroughly cleaned using isopropyl
122 alcohol (IPA) and inspected under a microscope. The pressure ring, clamp, and base
123 plate were printed using a 3D printer (Ultimaker 2+ extended, Utrecht). The exterior
124 dimensions of the PCB-SAW device are 120 mm (L)×120 mm (W)×30 mm (H).

Additionally, two localised pressers for focusing clamping force onto IDE region and a round holder for supporting the $LiNbO_3$ wafer, were also printed.

The assembly process is shown in Fig. 2b. The $LiNbO_3$ wafer was placed onto the round holder and its reference flat edge was aligned to be parallel with IDEs to ensure that the SAW generation was in the direction of the X direction of the $LiNbO_3$. The PCB was then placed on the $LiNbO_3$ wafer with the IDEs facing down. The clamp was mounted to the PCB and bolted to the base plate by slightly fastening the four screws. The pressure ring was screwed into the clamp to provide localised force to the PCB via the localised pressers and then the four screws were fully tightened. There was an observation window on the base plate for light transmission during microscopic measurement. A PDMS microchannel with the channel dimensions of 200 μm (L) × 100 μm (W) × 60 μm (H) was bonded to the $LiNbO_3$ wafer using plasma treatment before the above assembly. Tubing was connected to the inlet and the outlet of the single channel. Fig. 2c shows the assembled PCB-SAW device.

To study the reliability of the assembly, the PCB-SAW device was thoroughly characterised by using *s*-parameters and power transmission test. Details of the electrical characterisation can be found in the Supplementary Information, in which the working frequency is identified and matching networks (MNs) are recommended to couple the power amplifier and the PCB-SAW device to maximise power transmission.

PCB-SAW test with droplet actuation

The device is purely integrated by mechanical clamping and the contact quality between the PCB and the $LiNbO_3$ wafer is associated with the clamping force produced by the bolt torque (Fig. 2b). A droplet actuation test was performed to investigate the relationship between the clamping force and SAW generation indicated by droplet movement. The $LiNbO_3$ substrate was coated with a hydrophobic substance CYTOP™ (AGC Chemicals Europe), which was done by evenly distributing across the $LiNbO_3$ substrate[38].

For the clamping test, the clamping force between the $LiNbO_3$ substrate and the PCB IDEs was increased by adjusting the torque of the M5 screw torque on top of the localised pressers. A digital torque screwdriver (5-50 cNm, Adema, Taiwan) with a digital display was used to apply and read the torque. The torque was converted to clamping force by $F = \frac{T}{cD}$, where F, c,D and T correspond to clamping force (N), coefficient of friction, screw diameter (m) and torque (Nm), respectively. The standard value c for unlubricated steel is equal to 0.2. The readability of the digital torque screwdriver was 0.05 Nm, which allowed a minimum reading of the clamping force of 50 N. The VNA was used to monitor the real-time S_{11} while fastening the bolt. During each assembly, the clamping was adjusted so that the same minimum S_{11} value was achieved. This process facilitated establishing a correlation between the S_{11} and the clamping force, which allowed the use of S_{11} rather than the clamping force to guide the assembly.

Under each measured torque, a 1-μL water droplet was pipetted onto the $LiNbO_3$ substrate 5 mm away from the first finger electrode. Then an input power of 1.26 W was applied to the PCB-SAW device to actuate the droplet. The slight location variance of droplet initial positions in each test is insignificant as the SAW attenuation in the $LiNbO_3$ substrate is negligible[39]. Even though the droplet was placed in nearly identical location before actuation, a variation in speed of droplet transportation can be observed on both the devices. We hypothesise that this could have been caused by slightly uneven CYTOP coating, coating deterioration, slight contact angle variance, droplet volume variation, or a combination of these factors. Therefore, the droplet actuation by SAW was repeated five times before changing to another clamping force. A camera was used to capture the droplet moving and a calibrated software Tracker (www.compadre.org/osp/) was applied off-line to analyse the droplet velocity for indicating SAW amplitude. The captured droplet videos were analysed frame by frame using the leading edge of the droplet, as the reference to determine the displacement of the same droplet. Any two consecutive frames could produce one velocity using the displacement multiplied by the framerate. Five consecutive frames after the droplet moved were used to get four velocities, which were averaged to get the mean droplet velocity. The pixel size and the frame rate of the camera system were 10 μm and 60 fps, respectively, resulting in a velocity resolution of 0.6 mm/s, which was sufficient for capturing droplet movement.

To benchmark the performance of the PCB-SAW device with the SAW device made by standard photolithography[1], another IDT made by the same $LiNbO_3$ substrate using

186 the conventional photolithography process in cleanroom was prepared using the identical
187 geometry as the PCB-SAW device. The cleanroom-made IDT (CR IDT) was also coated
188 with CYTOP™ for the droplet test.
189
190 **Sample preparations**
191 To demonstrate the PCB-SAW device capability in manipulating microparticles within
192 droplets, a 3-4 μL glycerol droplet (3 mm in diameter) was prepared on the $LiNbO_3$
193 substrate and 20 μm polystyrene microspheres were pipetted into the glycerol droplet
194 (concentration of ~18,000 / μL). An input power of 0.2 W was used for manipulating the
195 microspheres.
196 To demonstrate the PCB-SAW device in manipulating microparticles inside the
197 microchannel, 10 μm polystyrene microspheres were mixed with a custom media at a
198 volume ratio of 1:2.7. The custom media consisted of glycerol and phosphate-buffered
199 saline (PBS) with a volume ratio of 1:4.4, which was made to prevent particle deposition.
200 Before sample introduction, the microchannel was flushed with bovine serum albumin
201 (BSA) solution (water:BSA = 100:1, mass ratio) for 20 min at a flow rate of 20 μL/min. The
202 input power in this experiment was 0.5 W.
203 For cell manipulation, A5499 human non-small-cell lung carcinoma (NSCLC) cell lines
204 were grown in Dulbecco's modified eagle media and supplemented with L-Glutamine (200
205 mM at 1:100 dilution, Gibco), Penicillin/Streptomycin (10,000 U/mL at 1:100 dilution,
206 Gibco), and 10% foetal bovine serum (FBS) in 75-cm^3 cell culture flasks until their density

reached 1×10^7 /mL. The cells were harvested from the plastic surface by trypsinisation, and then concentrated by centrifugation (3500 rpm, 5 min) to 2×10^7 /mL. The input power was set to be ~1 W in the experiment.

Viability test

There were three sample groups for viability test: (1) SAW-on Group, in which the NSCLC cells were continuously run through the PCB-SAW device for 5 minutes under the input power of ~1 W and flow rate of 20 μL/min. (2) SAW-off Group, in which the cells were running through the PCB-SAW device at the same flow rate and duration without applying SAW. (3) Control Group, in which the cells were kept in a steady tube on an ice bath for the same period of time.

Acridine orange (AO, 30 μg/mL) and di-amino-phenyl-indole (DAPI, 100 μg/mL) were mixed at the volume ratio of 3:10 to prepare an AO-DAPI solution for cell staining. For both SAW-on and SAW-off Group, 100-μL sample in total was collected after 5 minutes, of which three 10-μL samples were taken out to mix with the AO-DAPI solution at the volume ratio of 5:1 to stain the cells. The three stained samples were then pipetted into three cell chambers on a cell counter slide for viability analysis using a cell counter (NucleoCounter® NC-3000™). For the Control Group, the same amount of the sample was taken for staining and viability test. All the tests were repeated three times.

Results and discussion

Characterisation of the PCB-SAW device

The average width and spacing of the finger electrodes on the PCB were measured to be 38.7 μm and 61.1 μm, respectively (Fig. S1), which led to a SAW wavelength of 199.6 μm. The MNs were designed for the PCB-SAW device, which managed to reduce the device's reflection coefficients to -18.4 dB and -21.4 dB (Fig. S2c) and improve the transmission coefficients to -11.9 dB (Fig. S2e).

Under the unique clamping bonding of the PCB-SAW device, Fig. 3a shows the $|S_{11}|$ and droplet velocity against the clamping force. Despite large variance of SAW amplitude indicated by the droplet velocity, the optimal clamping force of 50 N produced the minimum S_{11} of -46 dB and the maximum average droplet velocity of 24.4 mm/s. Further increase in the clamping force to the PCB-SAW device decreased the $|S_{11}|$, the SAW amplitude and its variance. The reduction of the droplet velocity at a higher clamping force could be a result of over compressing the piezoelectric material, thus resulting in reduced SAW amplitudes or higher power reflection. The use of the MNs improved the sensitivity of the S_{11} reading, which allowed to easily achieve an optimal clamping assembly by reading the real-time S_{11} spectrum.

Once the optimal state of the PCB-SAW device was achieved by applying the clamping force of 50 N, the S_{11} spectrum was compared with that of the CR IDT with the same specifications as shown in Fig. 3b. It can be observed that the minimum S_{11} for both the

devices had a difference of ~0.21 MHz, which could be caused by the errors in the PCB manufacture and the parasitic capacitance and inductance introduced by the MN circuits.

Benchmarking the PCB-SAW device at the optimal state with the CR IDT in terms of actuating droplets under a range of input powers is shown in Fig. 3c. The CR IDT showed higher efficiency in converting the input power to SAW comparing with the PCB-SAW device. This is reasonable as the electrodes for the PCB-SAW device were mechanically clamped onto the piezoelectric substrate resulting in an imperfect signal coupling. This issue can be easily compensated by doubling input power to the PCB-SAW device. For example, operating the CR IDT at ~0.6 W drives the droplet velocity of 20 mm/s, which can be achieved by the PCB-SAW device working at ~1.2 W.

Manipulation of microparticles

SAW devices have been previously demonstrated in manipulating microparticles within droplets for sample mixing[38,40]. On the PCB-SAW device, a droplet sample containing polystyrene microspheres was placed at the centre between the two IDTs (Fig. 4a). When one of the IDTs was activated, a streaming pattern with two major vortices was observed (Fig. 4b, Video S1), which was in good agreement with the pattern formed on conventional SAW devices[40]. When both the IDTs were activated, a four-vortex streaming pattern was generated (Fig. 4c, Video S2), which again agreed with that produced on conventional SAW devices[38]. Each of the IDT in the tests was driven by an input power of 0.2 W.

Further tests using the PCB-SAW device as an acoustic tweezer were performed by introducing polystyrene microspheres into the PDMS microchannel. The acoustofluidic model of the PCB-SAW device was developed to study acoustic pressure distribution and predict the microparticle trajectories as shown in Fig. S5, which was adopted from conventional SAW device modelling[25,26].

A polystyrene microsphere sample was injected into the microchannel. After an evenly dispersed pattern was formed within the microchannel (Fig. 5a), RF signals with the same phase ($\Delta\varphi=0°$) were applied to both IDTs to produce SSAWs with the PNs located at the centre and near the two walls, which trapped microspheres to form three aggregation traces as shown in Fig. 5b and Video S3. By applying a 180° phase difference ($\Delta\varphi=180°$) to the RF signal driving one of the IDTs, ANs were formed at the centre and near the two walls, resulting in four microsphere traces as shown in Fig. 5c and Video S4. Both these cases show good agreements with the simulation results (Fig. S5).

Manipulation of cancer cells

To validate the manipulation of cells and test the biocompatibility, the PCB-SAW device was filled by the NSCLC cell sample (Fig. 6a) and repeated the same operation for microspheres. Applying RF signals with $\Delta\varphi=0°$ and $\Delta\varphi=180°$ to the two IDTs resulted in the formation of three-cell column (Fig. 6b, Video S5) and four-cell column (Fig. 6c, Video S6), respectively. The results demonstrated that the PCB-SAW device can be used as an

acoustic tweezer to manipulate and re-position cells controlled by changing RF signal phase.

The ability of the PCB-SAW device in preserving cell viability was tested using three sample groups, including Control, SAW-off and SAW-on. The results shown in Fig. 6d denote the viabilities of 98.2±0.8% (average ± SD), 97.6±1.2% and 96.9±0.6%, respectively. The analysis of variance showed no significant differences among these three groups (p = 0.166).

Conclusion

In this paper, we demonstrated that the novel PCB-SAW device is capable of performing all the functions realised using the standard SAW devices. The PCB-SAW has the main advantages of easy fabrication and low-skill entry requirement. The systematic characterisation to the PCB-SAW device and the comparison with the standard SAW device confirm the new technique has similar ability in actuating droplets. The PCB-SAW device can also be used as an acoustic tweezer to pattern microspheres and cells in a controllable manner, while maintaining high cellular viability.

Acknowledgements

The authors would gratefully acknowledge the financial support from EPSRC (EP/P002803/1, EP/P018998/1), EPSRC IAA, Welcome Trust, Global Challenges

Research Fund (GCRF), the Royal Society (IEC\NSFC\170142, IE161019), and the Natural Science Foundation of China (NSFC) (Grant No. 51811530310),

References

1. X. Ding, Z. Peng, S.-C. S. Lin, M. Geri, S. Li, P. Li, Y. Chen, M. Dao, S. Suresh and T. J. Huang, Cell separation using tilted-angle standing surface acoustic waves, *PNAS*, 2014, **111**, 12992–12997.
2. J. Shi, H. Huang, Z. Stratton, Y. Huang and T. J. Huang, Continuous particle separation in a microfluidic channel via standing surface acoustic waves (SSAW), *Lab on a Chip*, 2009, **9**, 3354.
3. M. Wu, Z. Mao, K. Chen, H. Bachman, Y. Chen, J. Rufo, L. Ren, P. Li, L. Wang and T. J. Huang, Acoustic Separation of Nanoparticles in Continuous Flow, *Advanced Functional Materials*, 2017, **27**, 1606039.
4. Y. Chen, M. Wu, L. Ren, J. Liu, P. H. Whitley, L. Wang and T. J. Huang, High-throughput acoustic separation of platelets from whole blood, *Lab Chip*, 2016, **16**, 3466–3472.
5. P. Li, Z. Mao, Z. Peng, L. Zhou, Y. Chen, P.-H. Huang, C. I. Truica, J. J. Drabick, W. S. El-Deiry, M. Dao, S. Suresh and T. J. Huang, coustic separation of circulating tumor cells, *PNAS*, 2015, **112**, 4970–4975.

6. K. K. Zeming, N. V. Thakor, Y. Zhang and C.-H. Chen, Acoustic impedance based size-independent isolation of circulating tumour cells from blood using acoustophoresis, *Lab on a Chip*, 2016, **16**, 75–85.

7. M. Wu, Y. Ouyang, Z. Wang, R. Zhang, P.-H. Huang, C. Chen, H. Li, P. Li, D. Quinn, M. Dao, S. Suresh, Y. Sadovsky and T. J. Huang, Isolation of exosomes from whole blood by integrating acoustics and microfluidics, *Proc. Natl. Acad. Sci. U.S.A.*, 2017, **114**, 10584–10589.

8. M. Wu, C. Chen, Z. Wang, H. Bachman, Y. Ouyang, P.-H. Huang, Y. Sadovsky and T. J. Huang, Separating extracellular vesicles and lipoproteins via acoustofluidics, *Lab Chip*, 2019, **19**, 1174–1182.

9. S. Li, X. Ding, Z. Mao, Y. Chen, N. Nama, F. Guo, P. Li, L. Wang, C. E. Cameron and T. J. Huang, Standing surface acoustic wave (SSAW)-based cell washing, *Lab Chip*, 2015, **15**, 331–338.

10. B. Ayan, A. Ozcelik, H. Bachman, S.-Y. Tang, Y. Xie, M. Wu, P. Li and T. J. Huang, Acoustofluidic coating of particles and cells, *Lab Chip*, 2016, **16**, 4366–4372.

11. S. P. Zhang, J. Lata, C. Chen, J. Mai, F. Guo, Z. Tian, L. Ren, Z. Mao, P.-H. Huang, P. Li, S. Yang and T. J. Huang, Digital acoustofluidics enables contactless and programmable liquid handling, *Nature Communications*, 2018, **9**, 2928.

12. J. Zhang, S. Yang, C. Chen, J. H. Hartman, P.-H. Huang, L. Wang, Z. Tian, P. Zhang, D. Faulkenberry, J. N. Meyer and T. J. Huang, Surface acoustic waves

enable rotational manipulation of Caenorhabditis elegans, *Lab Chip*, 2019, **19**, 984–992.

13. J. P. Lata, F. Guo, J. Guo, P.-H. Huang, J. Yang and T. J. Huang, Surface Acoustic Waves Grant Superior Spatial Control of Cells Embedded in Hydrogel Fibers, *Adv. Mater. Weinheim*, 2016, **28**, 8632–8638.

14. I. Bernard, A. A. Doinikov, P. Marmottant, D. Rabaud, C. Poulain and P. Thibault, Controlled rotation and translation of spherical particles or living cells by surface acoustic waves, *Lab Chip*, 2017, **17**, 2470–2480.

15. K. Chen, M. Wu, F. Guo, P. Li, C. Y. Chan, Z. Mao, S. Li, L. Ren, R. Zhang and T. J. Huang, Rapid formation of size-controllable multicellular spheroids via 3D acoustic tweezers, *Lab on a Chip*, 2016, **16**, 2636–2643.

16. G. Liu, F. He, Y. Li, H. Zhao, X. Li, H. Tang, Z. Li, Z. Yang and Y. Zhang, Effects of two surface acoustic wave sorting chips on particles multi-level sorting, *Biomed Microdevices*, 2019, **21**, 59.

17. Z. Tian, S. Yang, P.-H. Huang, Z. Wang, P. Zhang, Y. Gu, H. Bachman, C. Chen, M. Wu, Y. Xie and T. J. Huang, Wave number–spiral acoustic tweezers for dynamic and reconfigurable manipulation of particles and cells, *Science Advances*, 2019, **5**, eaau6062.

18. F. Guo, Z. Mao, Y. Chen, Z. Xie, J. P. Lata, P. Li, L. Ren, J. Liu, J. Yang, M. Dao, S. Suresh and T. J. Huang, Three-dimensional manipulation of single cells using surface acoustic waves, *PNAS*, 2016, **113**, 1522–1527.

19. A. Ozcelik, J. Rufo, F. Guo, Y. Gu, P. Li, J. Lata and T. J. Huang, Acoustic tweezers for the life sciences, *Nature Methods*, 2018, **15**, 1021.

20. T. D. Nguyen, V. T. Tran, Y. Q. Fu and H. Du, Patterning and manipulating microparticles into a three-dimensional matrix using standing surface acoustic waves, *Appl. Phys. Lett.*, 2018, **112**, 213507.

21. H. Bruus, Acoustofluidics 1: Governing equations in microfluidics, *Lab on a Chip*, 2011, **11**, 3742.

22. H. Bruus, Acoustofluidics 2: Perturbation theory and ultrasound resonance modes, *Lab Chip*, 2012, **12**, 20–28.

23. H. Bruus, Acoustofluidics 7: The acoustic radiation force on small particles, *Lab on a Chip*, 2012, **12**, 1014.

24. H. Bruus, Acoustofluidics 10: Scaling laws in acoustophoresis, *Lab on a Chip*, 2012, **12**, 1578.

25. R. Barnkob, N. Nama, L. Ren, T. J. Huang, F. Costanzo and C. J. Kähler, Acoustically Driven Fluid and Particle Motion in Confined and Leaky Systems, *Physical Review Applied*, 2018, **9**, 014027.

26. N. Nama, R. Barnkob, Z. Mao, C. J. Kähler, F. Costanzo and T. J. Huang, Numerical study of acoustophoretic motion of particles in a PDMS microchannel driven by surface acoustic waves, *Lab Chip*, 2015, **15**, 2700–2709.

27. R. P. Moiseyenko and H. Bruus, Whole-system ultrasound resonances as the basis for acoustophoresis in all-polymer microfluidic devices, *Phys. Rev. Applied*, 2019, **11**, 014014.

28. K. Xu, C. P. Clark, B. L. Poe, J. A. Lounsbury, J. Nilsson, T. Laurell and J. P. Landers, Isolation of a Low Number of Sperm Cells from Female DNA in a Glass–PDMS–Glass Microchip via Bead-Assisted Acoustic Differential Extraction, *Anal. Chem.*, 2019, **91**, 2186–2191.

29. J. Kirschner, Surface Acoustic Wave Sensors (SAWS): Design for Application, *Microelectromechanical systems*, 2010, 11.

30. A. R. Rezk, J. R. Friend and L. Y. Yeo, Simple, low cost MHz-order acoustomicrofluidics using aluminium foil electrodes, *Lab Chip*, 2014, **14**, 1802–1805.

31. Z. Ma, A. J. T. Teo, S. H. Tan, Y. Ai and N.-T. Nguyen, Self-Aligned Interdigitated Transducers for Acoustofluidics, *Micromachines*, 2016, **7**, 216.

32. R. P. Hodgson, M. Tan, L. Yeo and J. Friend, Transmitting high power rf acoustic radiation via fluid couplants into superstrates for microfluidics, *Appl. Phys. Lett.*, 2009, **94**, 024102.

33. R. N. Dean, A. K. Rane, M. E. Baginski, J. Richard, Z. Hartzog and D. J. Elton, A Capacitive Fringing Field Sensor Design for Moisture Measurement Based on Printed Circuit Board Technology, *IEEE Transactions on Instrumentation and Measurement*, 2012, **61**, 1105–1112.

34. K. Chetpattananondh, T. Tapoanoi, P. Phukpattaranont and N. Jindapetch, A self-calibration water level measurement using an interdigital capacitive sensor, *Sensors and Actuators A: Physical*, 2014, **209**, 175–182.

35. V. Jain, T. P. Raj, R. Deshmukh and R. Patrikar, Design, fabrication and characterization of low cost printed circuit board based EWOD device for digital microfluidics applications, *Microsystem Technologies*, 2017, **23**, 389–397.

36. A. R. M. Syaifudin, S. C. Mukhopadhyay, P. Yu, M. J. Haji-Sheikh, C. Chuang, J. D. Vanderford and Y. Huang, Measurements and Performance Evaluation of Novel Interdigital Sensors for Different Chemicals Related to Food Poisoning, *IEEE Sensors Journal*, 2011, **11**, 2957–2965.

37. K. Park, H.-J. Suk, D. Akin and R. Bashir, Dielectrophoresis-based cell manipulation using electrodes on a reusable printed circuit board, *Lab on a Chip*, 2009, **9**, 2224.

38. Y. Q. Fu, J. K. Luo, N. T. Nguyen, A. J. Walton, A. J. Flewitt, X. T. Zu, Y. Li, G. McHale, A. Matthews, E. Iborra, H. Du and W. I. Milne, Advances in piezoelectric thin films for acoustic biosensors, acoustofluidics and lab-on-chip applications, *Progress in Materials Science*, 2017, **89**, 31–91.

39. A. J. Slobodnik, P. H. Carr and A. J. Budreau, Microwave Frequency Acoustic Surface-Wave Loss Mechanisms on $LiNbO_3$, *Journal of Applied Physics*, 1970, **41**, 4380–4387.

40. M. Alghane, B. X. Chen, Y. Q. Fu, Y. Li, J. K. Luo and A. J. Walton, Experimental and numerical investigation of acoustic streaming excited by using a surface

424 acoustic wave device on a 128° YX-LiNbO $_3$ substrate, *Journal of Micromechanics*

425 *and Microengineering*, 2011, **21**, 015005.

426

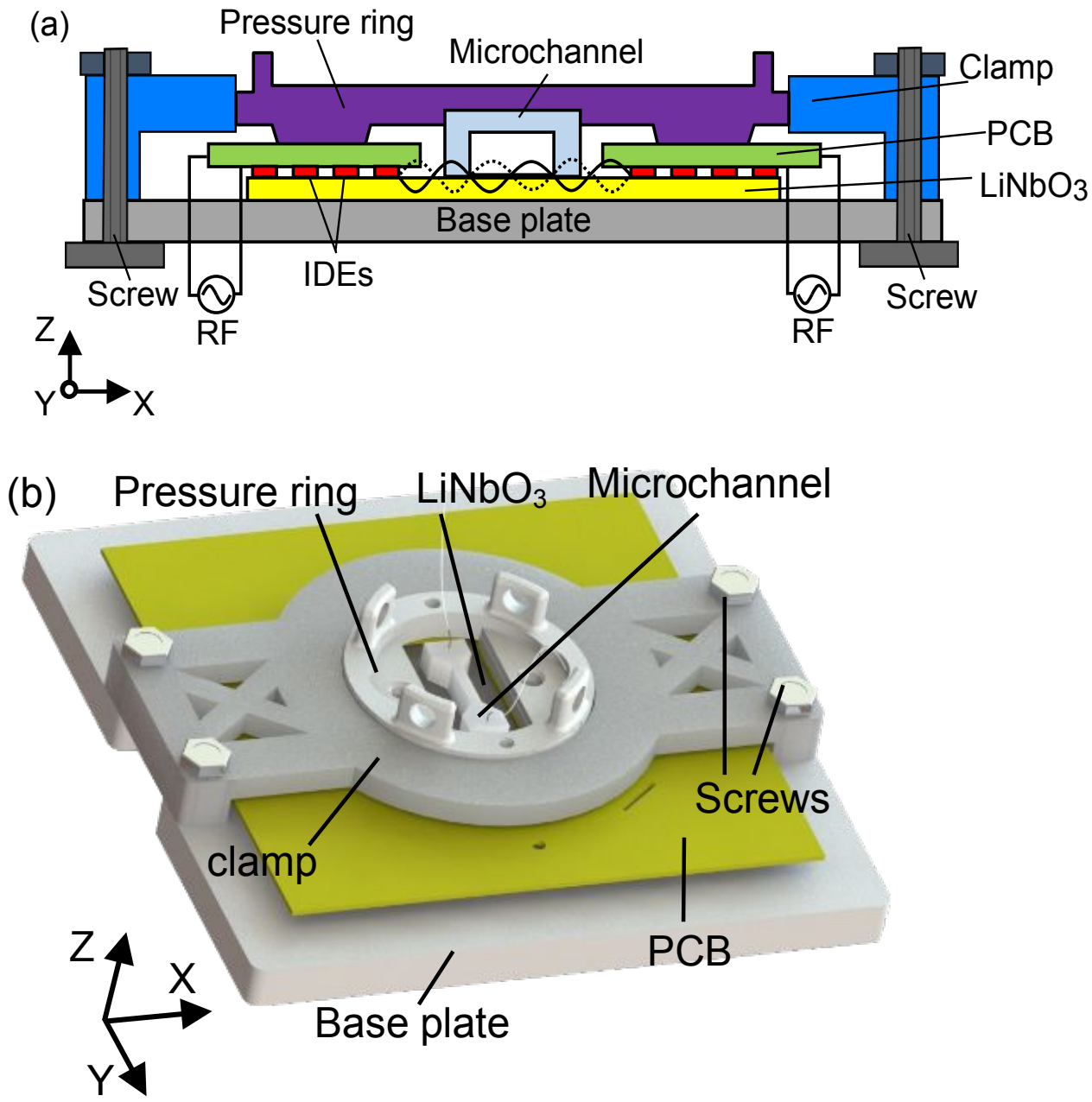

Figure 1. Schematic of the PCB-based surface acoustic wave (PCB-SAW) device. (a) Cross-sectional view of the PCB-SAW structure, consisting of a base plate, a clamp, a pressure ring, a PCB patterned with IDEs, a $LiNbO_3$ wafer and a microchannel. The PCB and the $LiNbO_3$ wafer are clamped by the mechanical jig to produce proximity for radio frequency signals coupling onto the wafer to produce SAW. (b) 3D model of the PCB-SAW device.

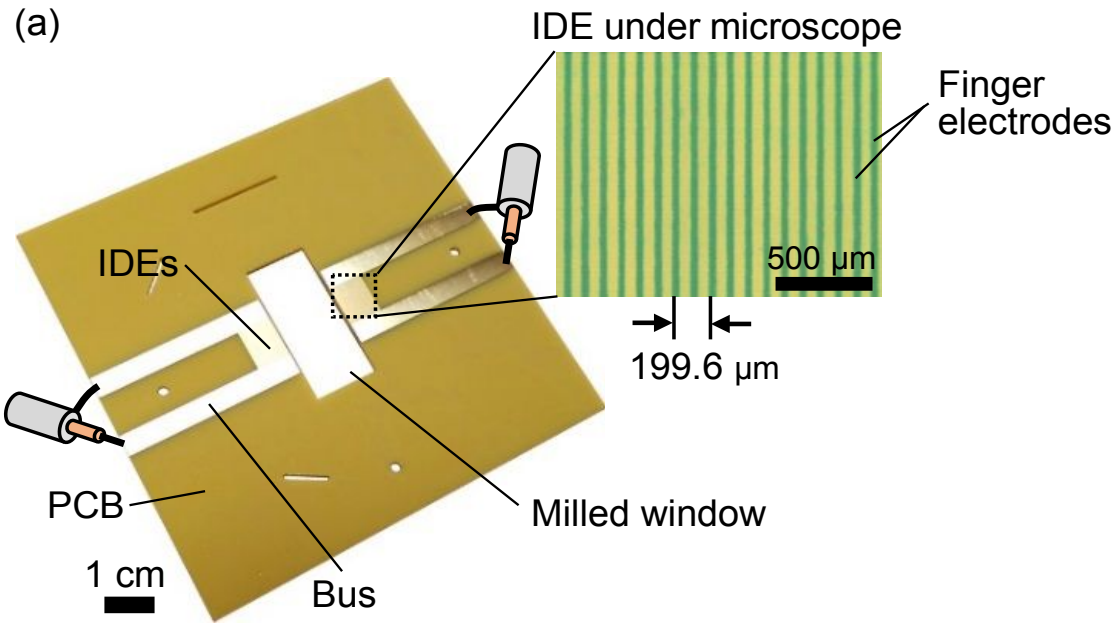
(a)
IDE under microscope
Finger electrodes
500 µm
199.6 µm
IDEs
PCB
1 cm
Bus
Milled window

10

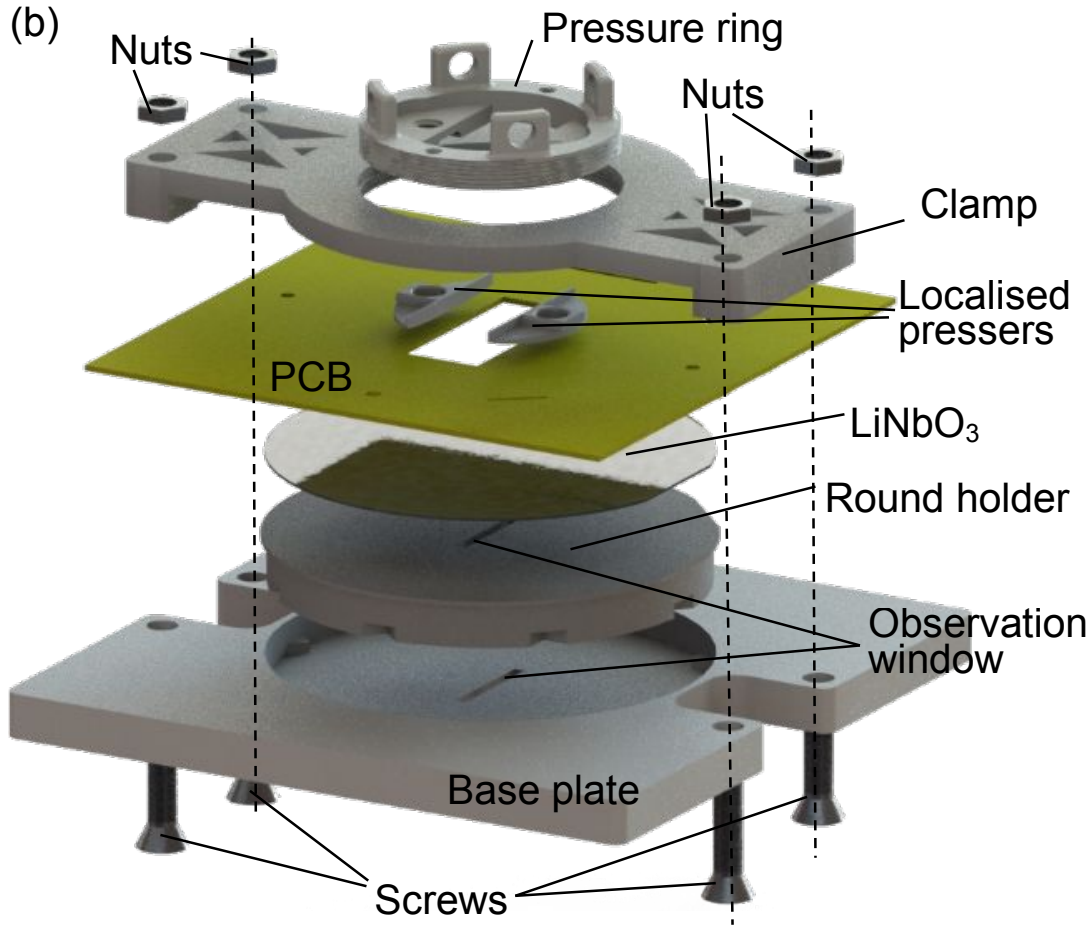
(b)
Nuts
Pressure ring
Nuts
Clamp
Localised pressers
PCB
LiNbO3
Round holder
Observation window
Base plate
Screws

11

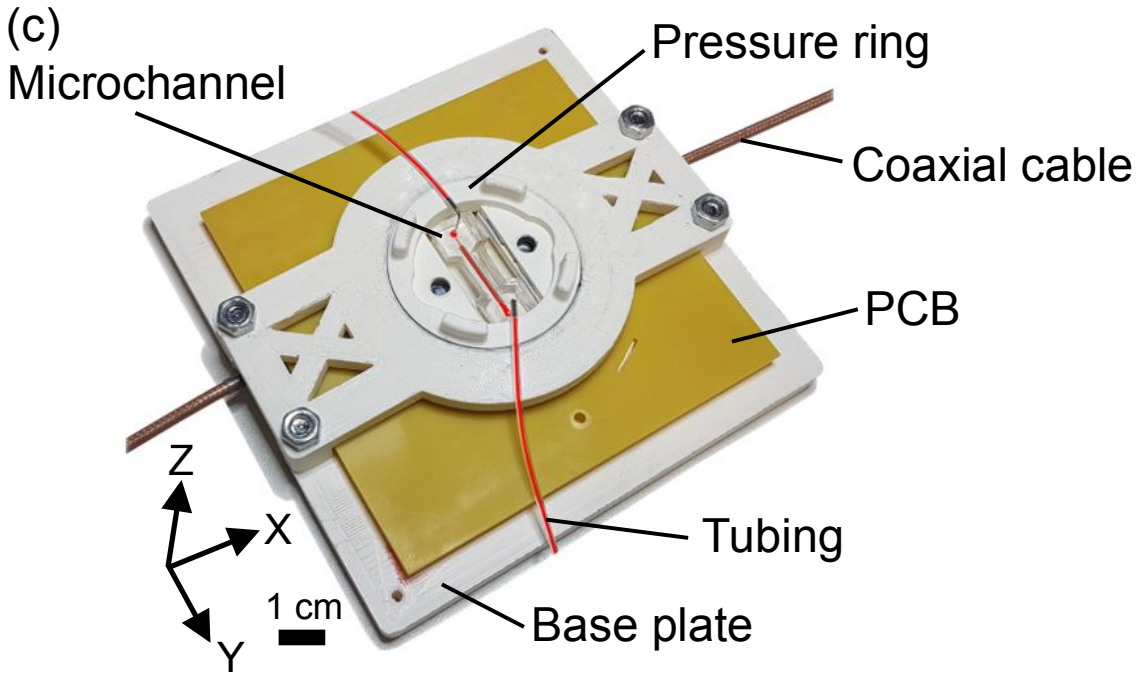

Figure 2. The components and assembly of the PCB-SAW device. (a) Pattern of the PCB and microscopic check of the IDEs on the PCB. (b) The assembly process of the PCB-SAW device. (c) The assembled PCB-SAW device.

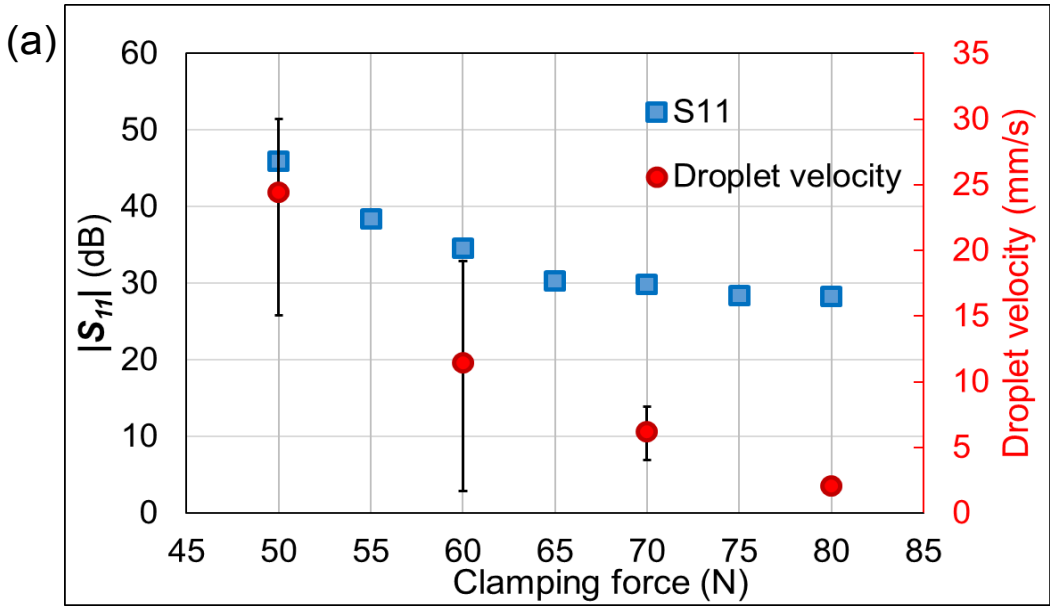
(a)
60
50
40
30
20
10
0
|S11| (dB)
35
30
25
20
15
10
5
0
Droplet velocity (mm/s)
S11
Droplet velocity
45
50
55
60
65
70
75
80
85
Clamping force (N)

17

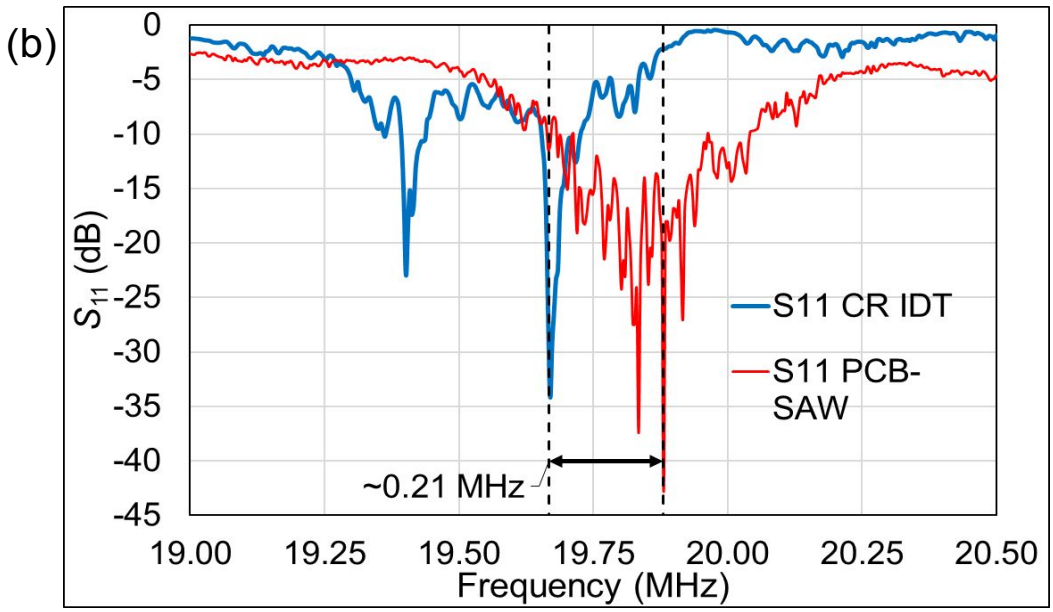
(b)
0
-5
-10
-15
-20
-25
-30
-35
-40
-45
S11 (dB)
S11 CR IDT
S11 PCB-SAW
~0.21 MHz
19.00
19.25
19.50
19.75
20.00
20.25
20.50
Frequency (MHz)

18

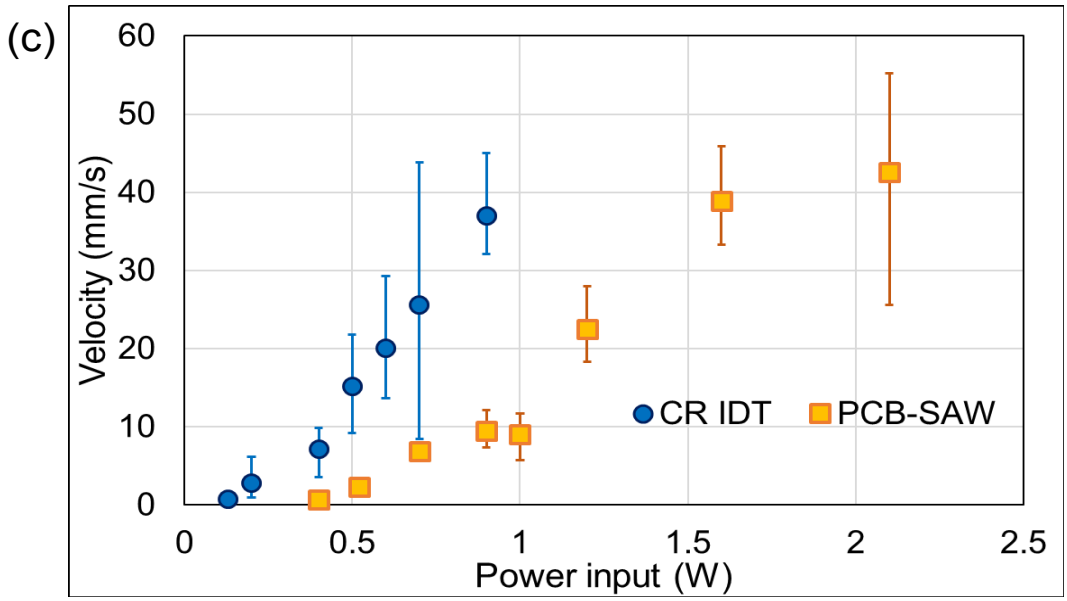

Figure 3. Characterisation of the PCB-SAW device and the comparations with the IDT made by photolithography in cleanroom (CR IDT). (a) The change of the S_{11} and the droplet velocity as the consequence of adding clamping force to the device. The droplet tests were done by applying an input power of 1.26 W. (b) Comparison between the S_{11} of the PCB-SAW device at 50 N and CR IDT, with the latter frequency being 19.67 MHz. (c) Comparation between the droplet velocities, which are driven by different input powers in the PCB-SAW device and CR IDT.

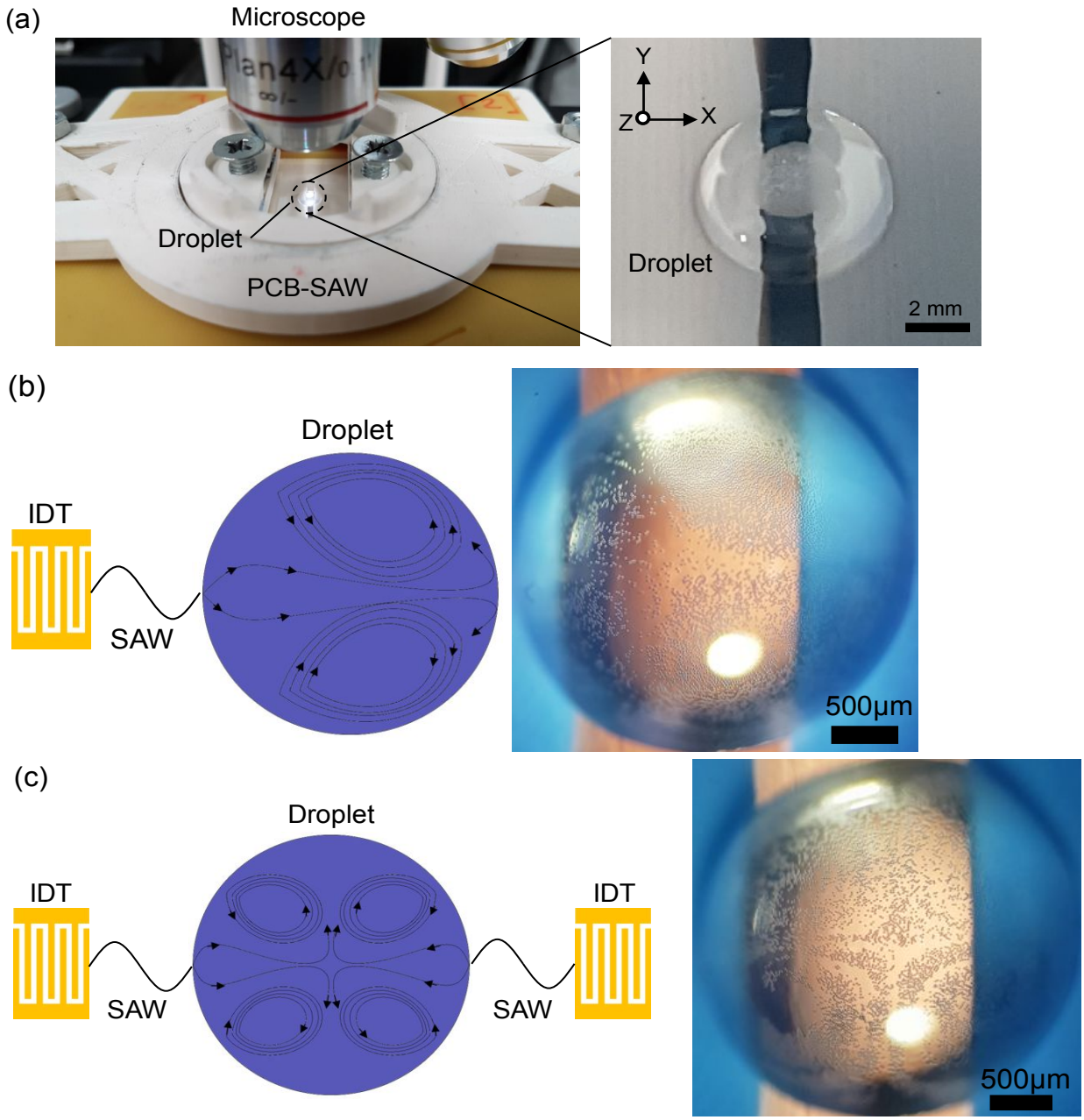

Figure 4. Testing the PCB-SAW device using droplet samples containing microspheres. (a) A droplet sample is applied to the PCB-SAW device at the centre of the two IDTs under a microscope. (b) A representation of the expected two-vortex streaming pattern and the experiment streaming pattern when one IDT is on (also in Video S1). (c) A representation of the expected four-vortex streaming pattern and the experiment streaming pattern when both IDTs are on (also in Video S2).

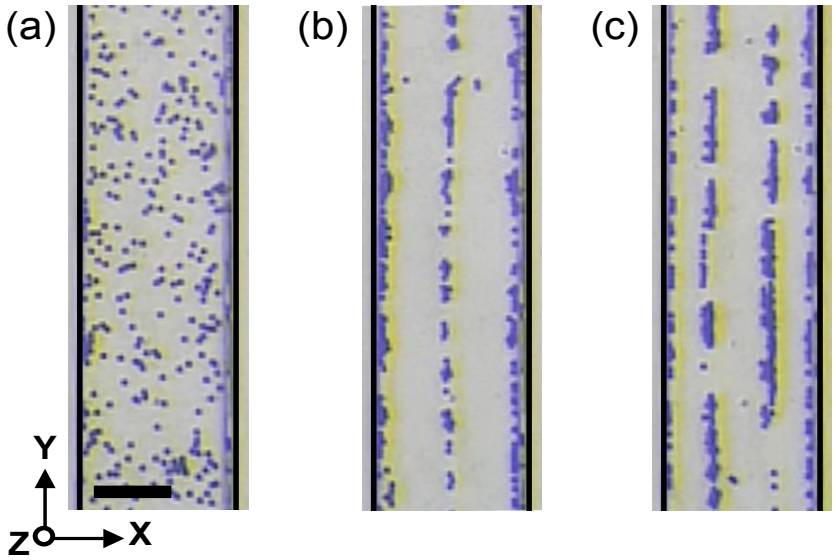

Figure 5. Particle trapping in the PCB-SAW device. (a) Microscopic image of 10 μm polystyrene microspheres evenly distributed inside the microchannel before applying SSAW. (b) Microscopic image of three microsphere traces inside the microchannel when applying SSAW with PNs located at the centre and near two sides of the microchannel. (c) Microscopic image of four microsphere traces inside the microchannel when applying SSAW with ANs located at the centre and near two sides of the microchannel. The scale bar is 100 μm.

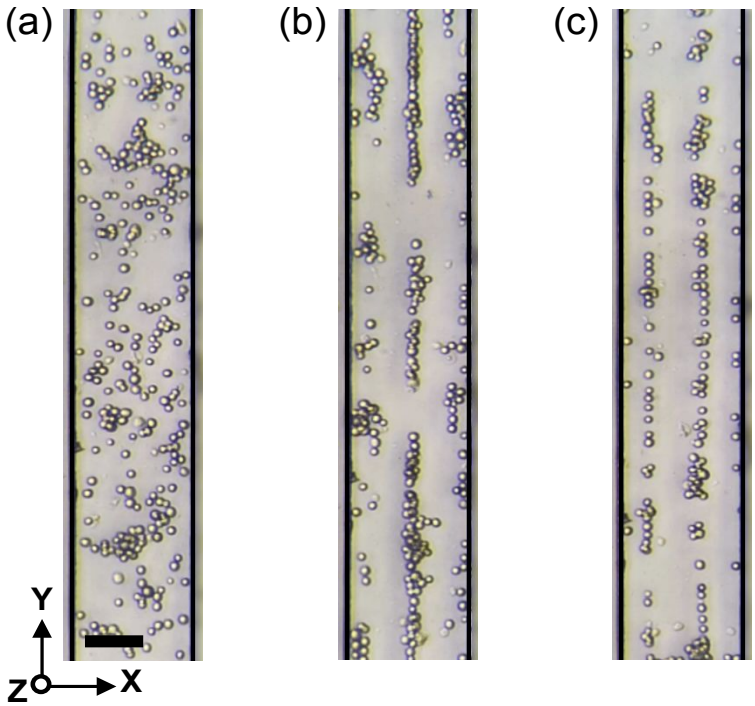

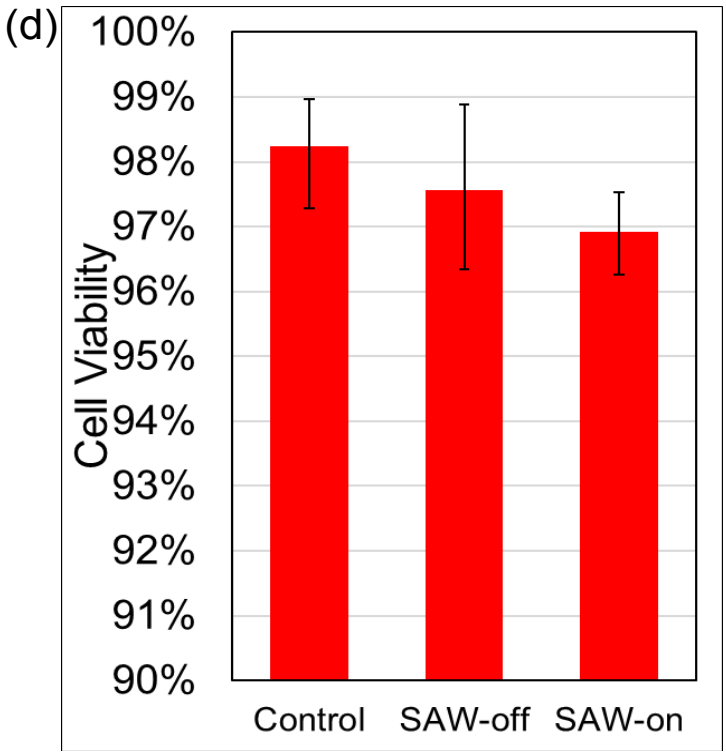

Figure 6. PCB-SAW manipulation of NSCLC cells. (a) Microscopic image of NSCLC cells evenly distributed inside the microchannel before applying SSAW. (b) Microscopic image of three cell traces inside the microchannel when applying SSAW with PNs located at the centre and near two sides of the microchannel. (c) Microscopic image of four cell traces inside the microchannel when applying SSAW with ANs

located at the centre and near two sides of the microchannel. The scale bar is 100 μm. (d) Cell viability test for Control, SAW-off and SAW-on Groups, no significant viability change was found.

Supplementary Information

Development and Characterisation of Acoustofluidic Devices Using Detachable Electrodes Made from PCB.

Roman Mikhaylov[1], Fangda Wu[1], Hanlin Wang[1], Aled Clayton[2], Chao Sun[3], Zhihua Xie[4], Dongfang Liang[5], Yinhua Dong[6], Fan Yuan[7], Despina Moschou[8], Zhenlin Wu[9], Ming Hong Shen[10], Jian Yang[10], Yongqing Fu[11], Zhiyong Yang[12], Christian Burton[1,2], Rachel J. Errington[2], Marie Wiltshire[2], Xin Yang[1]

[1] Department of Electrical and Electronic Engineering, School of Engineering, Cardiff University, Cardiff CF24 3AA, UK

[2] Tissue Micro-Environment Group, Division of Cancer & Genetics, School of Medicine, Cardiff University, Cardiff CF14 4XN, UK

[3] School of Life Sciences, Northwestern Polytechnical University, 710129, P.R. China

[4] Department of Civil Engineering, School of Engineering, Cardiff University, Cardiff CF24 3AA, UK

[5] Department of Engineering, University of Cambridge, Cambridge CB2 1PZ, UK

[6] Department of Neurology, Tianjin 4th Centre Hospital Affiliated to Nankai University, 300140, P.R. China

[7] Department of Biomedical Engineering, School of Engineering, Duke University, NC 27708-0281, USA

[8] Centre for Biosensors, Bioelectronics and Biodevices (C3Bio) and Department of Electronic & Electrical Engineering, University of Bath, Bath BA2 7AY, UK

[9] School of Optoelectronic Engineering and Instrumentation Science, Dalian University of Technology, 116023, P.R. China

[10] Preclinical Studies of Renal Tumours Group, Division of Cancer and Genetics, School of Medicine, Cardiff University, Cardiff CF14 4XN, UK

[11] Faculty of Engineering and Environment, Northumbria University, Newcastle Upon Tyne, Newcastle NE1 8ST, UK

[12] School of Mechanical Engineering, Tianjin University, 300072, P.R. China

S1. Mechanical characterisation of the IDE on PCB

The dimensions of the interdigital electrodes (IDEs) shown in Fig. 2a were measured using a calibrated reflected light microscope (KERN, Germany) with a 10× objective lens. The IDE width and spacing were found to be 38.7±3.1 µm (average ± SD) and 61.1±3.0 µm (average ± SD), respectively (Fig. S1, n = 161), resulting in a wavelength of 199.6±4.8 µm (average ± SD).

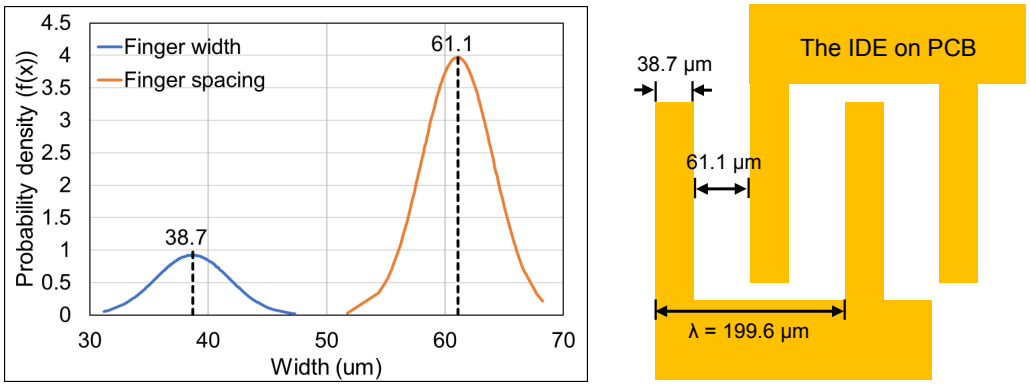

Supplementary Figure 1. The average width and spacing of finger electrodes on the PCB are 38.7 and 61.1, respectively (n = 161).

S2. Electrical characterisation

The left and right IDTs form a two-port network, as shown in Fig. S2a, whose *S*-parameters can be measured by using a vector network analyzer (VNA, E5061B ENA, Keysight) to indicate the contact between the PCB IDE and the $LiNbO_3$ wafer. The VNA measurements include: S_{11} – power reflection coefficient seen at the left IDT (Port 1), S_{21} - power transmission coefficient from the left to the right IDT (Port 1 to Port 2), S_{12} - power transmission coefficient from the right to the left IDT (Port 2 to Port 1), and S_{22} - power reflection coefficient seen at the right IDT (Port 2).

Because the contact between the PCB IDE and the $LiNbO_3$ wafer was formed by mechanical clamping, the power reflections from both Port 1 and Port 2 are high which could result in inefficient power transmission between the RF power amplifier and the PCB-SAW device. To counteract this, an impedance matching network (MN)[1] as shown in Fig. S2b was developed for both the left and the right IDTs to bring their impedances close to 50 Ω. Fig. S2c shows the S_{11} and S_{22} of the PCB-SAW device with and without the use of the MNs, which denotes a significant reduction on reflection from -2.7 dB to -18.4 dB and from -1.7 to -21.4 dB, respectively ('_MN' is the parameter with addition matching network in all figures. Fig. S2d shows the Smith charts of

both IDTs with and without MN, which proved that the impedances of the two IDTs were significantly improved towards 50 Ω by adding MNs. To understand the insertion loss of the PCB-SAW device, transmission coefficients, S_{12} and S_{21}, were also measured as the result shown in Fig. S2e, which also confirmed that the added MNs improve power transmission from one IDT to the opposite one.

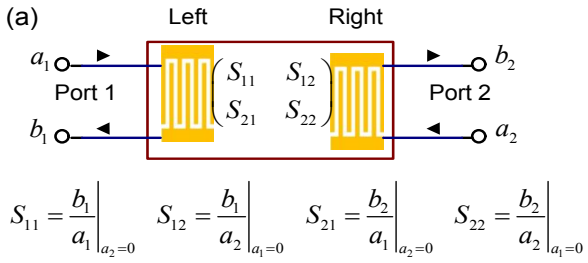

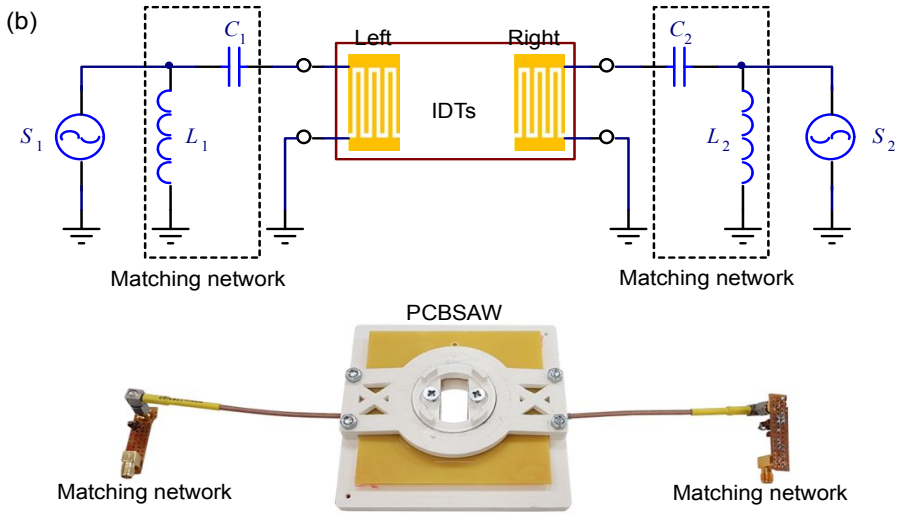

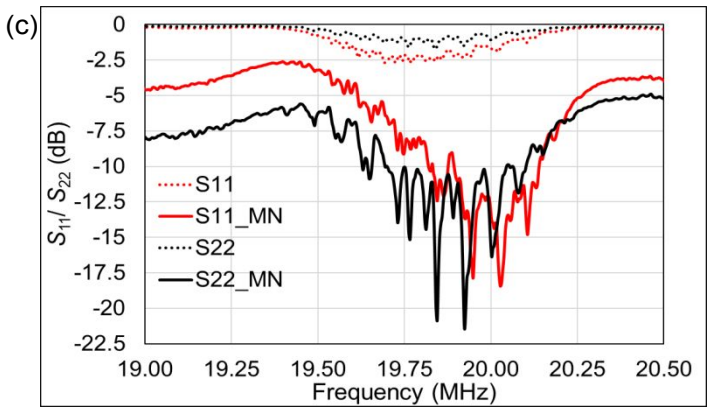

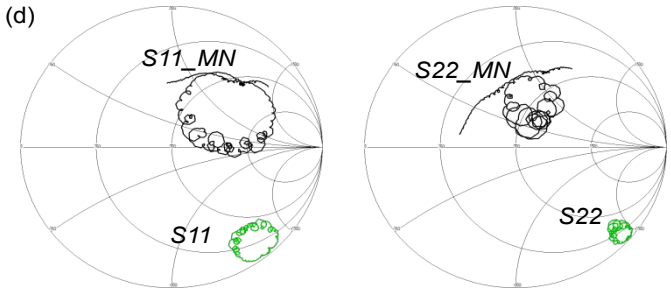

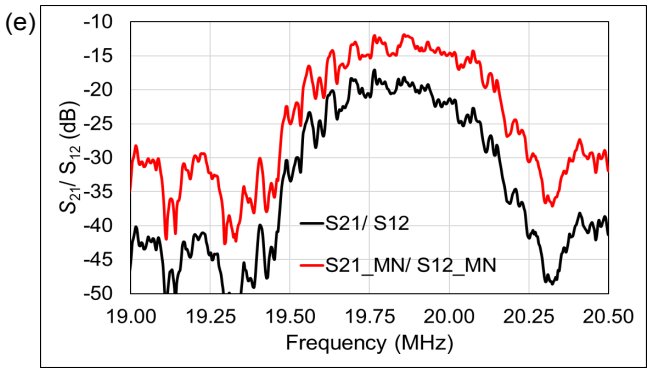

Supplementary Figure 2. Electrical characterisation to the PCB-SAW device. (a) Equivalent circuit of the two-port PCB-SAW device and the *S*-parameters. (b) Matching networks are added to couple the PCB-SAW device to RF signals. (c) Reflection coefficients of the PCB-SAW device with and without the use of matching networks. (d) Smith charts of the PCB-SAW device with and

without the use of matching networks. (e) Transmission coefficients of the PCB-SAW device with and without the use of matching networks.

To test the stability and repeatability of the PCB-SAW assembly and the readout of Rayleigh mode frequency from *S*-parameter measurements, the device was assembled and disassembled multiple times (n=23). The Rayleigh mode frequency was identified at which the S_{11}/S_{22} was minimum or S_{12}/S_{21} was maximum. As shown in Fig. S3a, in general, the addition MNs slightly increased the average Rayleigh mode frequency. For the frequency readout from S_{11} and S_{22}, the average frequencies moved from 19.77±0.08 MHz (average ± SD) to 19.82±0.13 MHz, and from 19.80±0.10 MHz to 19.89±0.11 MHz, respectively. While for S_{12} or S_{21}, the average frequency moved from 19.82±0.06 MHz (average ± SD) to 19.85±0.04 MHz. The observed frequency shift was induced because of the additional inductance and capacitance introduced by the MNs. Furthermore, the average reflection coefficients were consistently reduced from -2.7 dB to -25.2 dB, and from -2.4 dB to -27.8 dB, respectively, as shown in Fig. S3b. Similar improvement produced by the MNs also happened to the transmission coefficients as the measurement results shown in Fig. S3c, from -18.1 dB to -12.1 dB. The assembly and disassembly tests confirmed that the change to the Rayleigh mode frequency of the PCB-SAW device was within a small range, which allowed a stable SAW wavelength to produce for applications. Generally, the use of MNs improved the electrical characteristics of the PCB-SAW device.

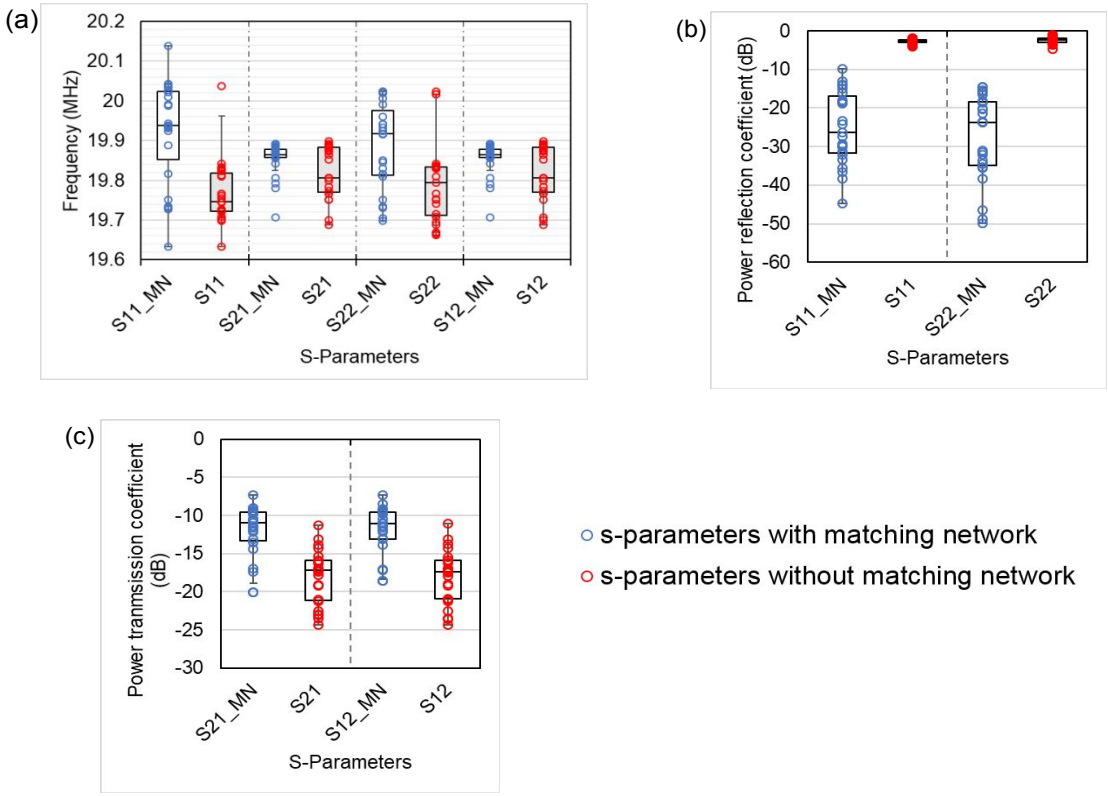

Supplementary Figure 3. *S*-parameter characterisation of the PCB-SAW device. (a) The readout of Rayleigh mode frequencies from $S_{11,}$ $S_{22,}$ S_{21} and S_{12} measurements with and without the MNs. (b) The reflection coefficients of the PCB-SAW device with and without the MNs. (c) The transmission coefficients of the PCB-SAW device with and without the MNs.

To find out which working frequency identified from the readout of *S*-parameters produced the optimal power transmission, the device was then configured in the measurement as the setup shown in Fig. S4a, in which a coupler was used to couple the RF signal to the PCB-SAW device while interfacing with two power meters (PM_1 and PM_2) to monitor the incident and reflected powers of one IDT. The difference between the incident and reflected powers was the input power of the device. A third power meter (PM_3) was connected to the opposite IDT to measure the transmitted power. By using four different working frequencies determined by the readout of the four *S*-parameters, the transmitted powers were recorded as shown in Fig. S4b and S4c. Generally, the addition MNs improved the power transmission in all cases, and the working frequency determined by the readout of S_{21} or S_{12} showed the largest power transmission.

To prove that the optimal working frequency determined by the readout of S_{21} or S_{12} was reliable, the input power was fixed at -10 dBm while the input frequency was tuned slightly above and below the optimal working frequency. As shown in Fig. S4d, the transmitted power recorded by the power meter informed that the maximum power transmission took place at 19.871 MHz, which was in a good agreement with the readout from S_{21} or S_{12}. The result indicated that one can use the VNA readout of S_{21} or S_{12} to predict the optimal working frequency of the PCB-SAW device.

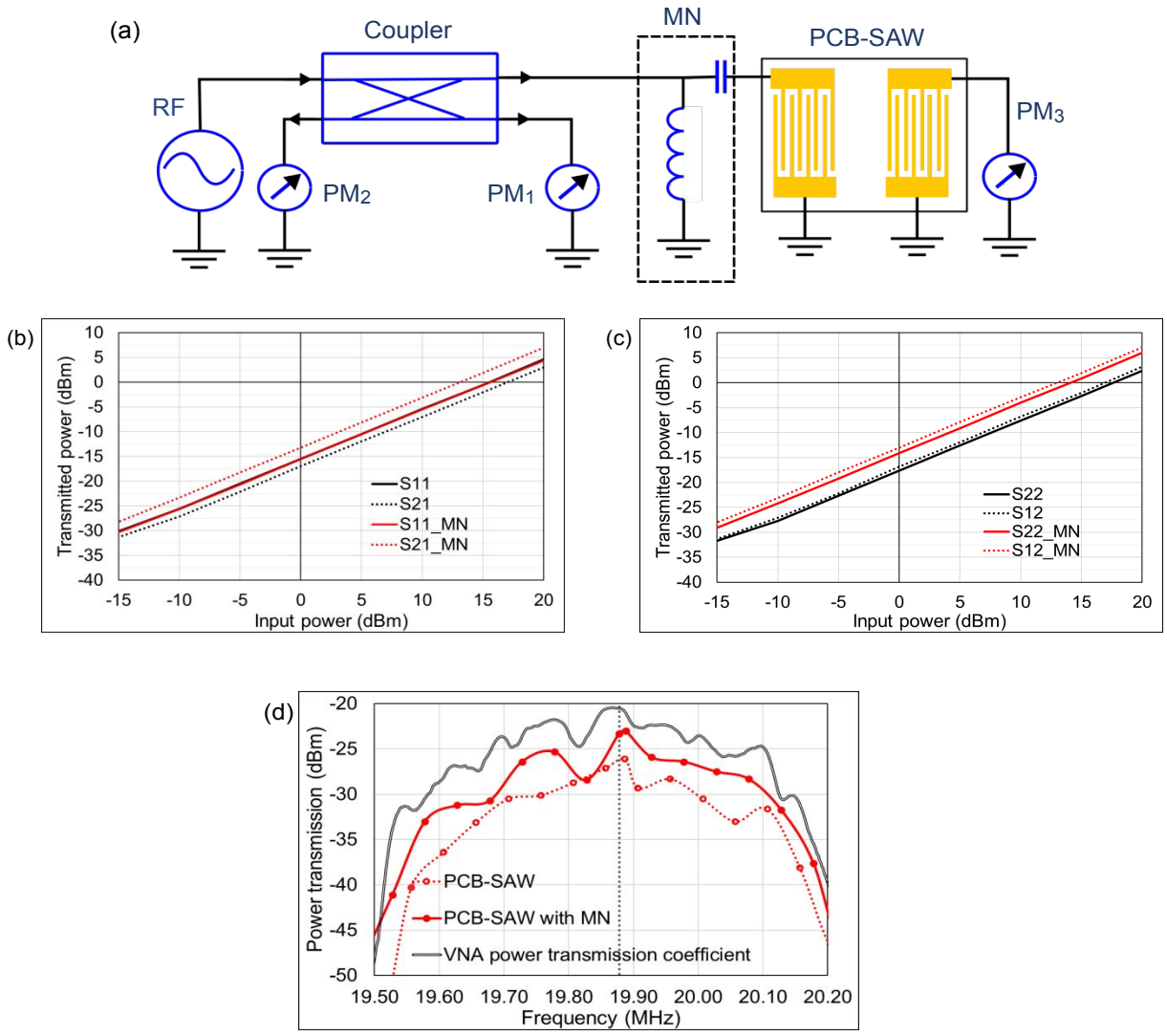

Supplementary Figure 4. Investigation of the power operation and determination of the optimal working frequency for the PCB-SAW device. (a) The measurement setup of the power transmission test. (b) and (c) The transmitted power versus input power at different working frequencies identified by readouts of four *S*-parameters. (d) The agreement on the optimal working

frequency between the power transmission measurement and the VNA readout. The vertical dotted line indicates the frequency from S_{21} readout.

S3. The PCB-SAW device modelling

To study the distribution of acoustic pressure and predict microparticle trajectories in the PCB-SAW device, COMSOL Multiphysics® was used to compute the numerical results on the X-Z plane of the microchannel. Figs. S5a and S5b show the distribution of the acoustic pressure when pressure node (PN) and pressure anti-node (AN) formed at the centre of the microchannel, respectively. Particle trajectories corresponding to both conditions are given in Figs. S5c and S5d, respectively. The first case indicates three particle aggregation traces (red dots in Fig. S5c) on the plane, two of which are close to the walls of the microchannel. The second case creates a more complex particle aggregation traces on the plane. It is worth noting that the particle aggregation at the centre (the yellow dot in Fig. S5d) is unstable due to the occurrence of force imbalance, i.e. $\sum \boldsymbol{F}_x \neq 0$, thus in reality microparticles migrated to the centre tend to be attracted towards adjacent stable PN locations (pointed by green and black arrows), resulting in low probability of trapped microparticles in the centre, which is in a good agreement with microsphere and cell experiments. In addition, two approximated aggregation traces (pointed by green or black arrows) are expected to form a combined particle trace under microscope.

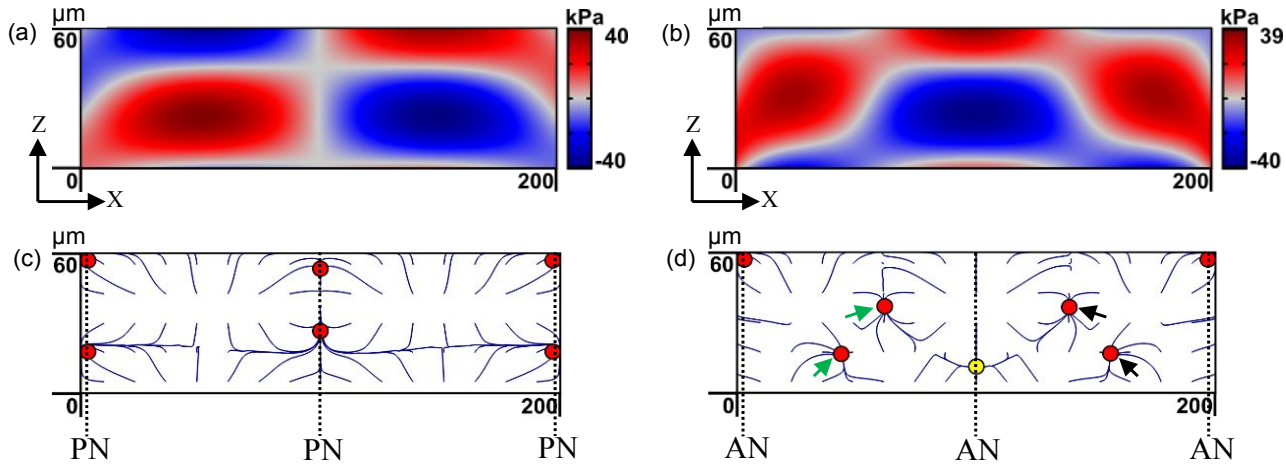

Supplementary Figure 5. COMSOL Multiphysics® simulation of the PCB-SAW device. (a) Acoustic pressure when PN located at the centre of the microchannel. (b) Acoustic pressure when

AN located at the centre of the microchannel. (c) Particle trajectories for PN located at the centre of the microchannel. (d) Particle trajectories for AN located at the centre of the microchannel.

References

1. Lackey, J. E. *Fundamentals of electricity and electronics. 579p.* (Holt Rinehart, 1983).